



Mg-based metallic glass nanowires with excellent photothermal effect

Jinbiao Huang, Jianan Fu, Luyao Li, Jiang Ma^{*}

Shenzhen Key Laboratory of High Performance Nontraditional Manufacturing, College of Mechatronics and Control Engineering, Shenzhen University, Shenzhen, 518060, China

ARTICLE INFO

Keywords:

Mg-based metallic glass
Biocompatible nanowires
Thermoplastic forming
Photothermal effect

ABSTRACT

Metallic nanostructures are important for the research and application of photothermal effects, especially in the emerging field of photothermal therapy, where metallic glasses (MGs) are promising candidates. However, the currently prepared nanostructures mainly focus on noble metal-based MGs systems with excellent thermoplastic forming ability, while less research has been done on the nanostructure fabrication of biocompatible systems. Here we demonstrate that the diameter-adjustable and biocompatible Mg-based MG nanowires can be successfully fabricated. Nanowires exhibit excellent photothermal effects due to their unique structure, which is important for photothermal therapy. Under the irradiation of 2 W cm^{-2} power laser, the maximum temperature of nano-engineered surface can reach $\sim 71 \text{ }^\circ\text{C}$ in a short time of about 20 s. The excellent photothermal imaging results were also demonstrated. This work opens a window not only to fabricate the low-cost MG nanowires, but to discover potential applications such as photothermal therapy, desalination and solar fuel etc.

Metallic nanostructures have unique physical and chemical properties, such as light absorption [1,2], catalysis [3–5], heat dissipation [6,7] *et al.* Nanostructures on metallic surfaces are of great significance for the study and application of photothermal effects, especially in the emerging field of cancer photothermal therapy, which requires the preparation of biocompatible nanostructured materials. Recent advancements in fabrication techniques have endowed researchers with tools to fabricate nanostructured materials, even on metallic surfaces. The techniques currently used to fabricate materials with nano-structures include lithography techniques [8,9], focused electron beam induced deposition [10,11], laser beam processing [12,13], *et al.* However, these technologies require sophisticated machining equipment and control systems, which are high-cost and the fabrication processes are complex. Therefore, there is a need for a mature and low-cost method to prepare nanostructured materials, especially metal nanomaterials. Thermoplastic forming (TPF) is a well-established process currently used for the preparation of MGs micro and nano structures [14–16], which has the advantages of short fabricating time, low-cost and the ability to prepare large-area micro and nano structures.

Amorphous alloys, also known as MGs, have received a lot of attention due to their excellent properties such as high strength [17,18], high hardness [19,20] and corrosion resistance. Compared with other traditional metallic materials, thermal plasticity is one of the most unique properties. It can be easily and precisely thermally formed due to

the viscous state in the temperature span between glass transition temperature (T_g) and crystallization temperature (T_x) [21–24]. In the previous studies, the MGs that have been used for fabricating micro and nano structures are mainly focus on Pt-based [25,26], Pd-based [27–29], Au-based [30]. Although these noble metal-based MGs have excellent TPF ability, the high-cost and bad biocompatibility greatly limited their broad applications. In recent years, the demand for biocompatible and functional materials has increased in the medical field [31,32], biosensors [33], bioelectronic systems [34]. Therefore, the development of MGs with better TPF ability for nano-structure, biocompatibility and low-cost can have the bright prospect.

In this work, the $\text{Mg}_{65}\text{Cu}_{25}\text{Y}_{10}$ MG (Mg-based MG) alloy of biocompatibility was chosen as the material and successfully fabricated Mg-based MG nanowires (Mg-based NWs) with different controllable diameters without change the amorphous nature of the samples after TPF. Additionally, the flow behavior of the NWs during the TPF process was investigated, which exhibited Newtonian fluid behavior. The MG surface with NWs exhibited sensitive photothermal response because of the construction of the NWs. Under the irradiation of 0.5 W cm^{-2} , 1 W cm^{-2} , 2 W cm^{-2} power near-infrared (NIR) 808 nm wavelength laser, the temperature can reach $35 \text{ }^\circ\text{C}$, $47 \text{ }^\circ\text{C}$, $71 \text{ }^\circ\text{C}$, respectively. Under the irradiation of 1 W cm^{-2} power laser, the maximum temperatures of NWs with diameters of 175, 221 and 290 nm were $\sim 50 \text{ }^\circ\text{C}$, $\sim 42 \text{ }^\circ\text{C}$ and $\sim 38 \text{ }^\circ\text{C}$. Furthermore, Mg-based MG has good biocompatibility [35,36], so it

^{*} Corresponding author.

E-mail address: majiang@szu.edu.cn (J. Ma).

has potential application in cancer photothermal therapy. When the letter patterns “SZU” were fabricated with Mg-based MG NWs, this surface rapidly became imageable. Our work may have discovered a new type of MG that can replace the precious metal matrix. This MG with excellent biocompatibility and photothermal response may have broad applications in solar cells, photothermal therapy and electromagnetic shielding. potential application prospects.

The $Mg_{65}Cu_{25}Y_{10}$ (at%) MG was used in present work due to its wide supercooled liquid region (SCLR) [37], TPF ability and potential biocompatibility. The Cu-Y intermediate alloy was prepared by arc melting of elements with purity greater than 99.99% under low-pressure vacuum environment of argon. The Mg (>99.995% purity) element was then added to the intermediate alloy ingot by induction melting to form the final ingot. To ensure full uniformity, each ingot was re-melted four times. Afterwards, the MG-plates with a thickness of 1.5 mm were obtained by spray casting the melting alloy into a copper mold. The prepared MG plates with a thickness of 1.5 mm were cut into small pieces with 5 mm diameter for TPF process.

Anodic aluminum oxide (AAO) [28] templates were purchased directly from commercial supplier and as templates to fabricate NWs on the Mg-based MG surface. Three types of AAO template with nano-scales holes diameter of about 169 nm, 231 nm and 282 nm were used in the experiment.

The polished $Mg_{65}Cu_{25}Y_{10}$ specimen was placed on the AAO template in the experimental mold. The sample was heated to 473 K and applied a pressure of 500 MPa and maintained the pressure for 20 s to fill the MG into the AAO template. At this temperature, the viscosity of Mg-based MG is lower, which is more conducive to TPF and ensures amorphous properties. Fig. 1 is a schematic diagram of the process of preparing NWs from Mg-based MG by TPF.

After that, the pressure was removed and the sample was taken out from the mold after cooled to room temperature. Finally, after the sample with NWs was released by dissolving the AAO templates off in 20 wt.% NaOH at 60 °C for 10 min, the Mg-based NWs were obtained.

The amorphous nature of Mg-based MG as cast and after TPF was verified by X-ray diffraction equipment (XRD; Rigaku MiniFlex600) with Cu K α radiation. The XRD patterns were acquired in a scanning angle 2θ range of 20°–80° at a scan rate of 10° per minute and a scan interval of 0.02°. The thermodynamic properties of Mg-based MGs, such as characteristic temperature T_g and T_x , were studied by differential scanning calorimetry (DSC; Perkin–Elmer DSC-8000) at continuous heating rates of 20 K /min under a flow of high purity argon. Morphology and elemental distribution of Mg-based MG NWs were observed by field scanning electron microscope (SEM; FEI QUANTA FEG 450). The heating rates and thermal images of the samples were obtained by an infrared thermal imager (Fotric 280d).

The morphology of the sample prepared by TPF is analyzed by SEM. Fig. 2 shows large area NWs of different sizes. Fig. 2(a)–(c) shows the SEM morphologies of NWs prepared with three different nano-pore sizes of AAO templates (pore sizes of about 169 nm, 231 nm and 282 nm). Fig. 2(d)–(f) show the high magnification SEM images. It can be seen that as the aspect ratio (length/diameter) of the NWs becomes larger, multiple NWs tend to clump together which may be due to reduced surface energy. The longer the nanowire length, the more obvious the agglomeration phenomenon. As shown in Fig. 2(g)–(i), the average diameters of the three NWs prepared by TPF with three AAO templates were 175.2 nm, 220.5 nm and 289.5 nm, respectively. Fig. 2(j) investigates the element release, and it can be found that the elements of the NWs are Mg, Cu, Y, and the three element releases are uniform and consistent with the elements in the materials used.

In order to characterize the amorphous properties of Mg-based MG before and after TPF, the XRD and DSC were used for the sample testing. Fig. 3(a) shows the XRD pattern of $Mg_{65}Cu_{25}Y_{10}$ MG with different diameters under TPF in the SCLR. It can be seen that the XRD pattern of the sample prepared by TPF only has typical diffuse scattering peak of amorphous structure, but does not have sharp crystal peaks. This indicates that the NWs prepared by TPF still maintain amorphous properties, without crystallization phenomenon.

The curves obtained by DSC were shown in Fig. 3(b) and the glass transition temperature and crystallization temperature statistics of different samples were shown in Table 1. From Table 1, it can be clearly seen that there is no obvious shift in the SCLR region, glass transition point and glass crystallization point before and after TPF. Mg-based MG has a wider SCLR width $\Delta T \approx 55$ °C. The wider SCLR indicates that Mg-based MG has better TPF ability to a certain extent. Fig. 3(c) shows the width and critical size of the SCLR of MG in different systems developed so far. The SCLR of Mg-based MG is smaller than Pd-based, Pt-based, Zr-based, La-based, but larger than Cu-based, Fe-based, Ni-based, Ca-based MG. Although common metals Zr-based and La-based have larger SCLR, their compositions generally contain toxic substances (such as Be and La [40]), so Mg-based MG is a better choice for photothermal therapy.

When the Mg-based MG is formed in the SCLR, the MG belongs to the Newtonian fluid state under heating [41]. Fig. 4(a) shows the release diagram of the force and velocity of the MG fluid in the nanopore template. The shape of the solid boundary of the template was changed suddenly, causing the internal structure of the amorphous fluid to be destroyed. The overall structure of the fluid needs to be readjusted to adapt to the new uniform flow conditions, and the vortex generated will lead to the generation of local resistance. The calculation formula of the local resistance loss is:

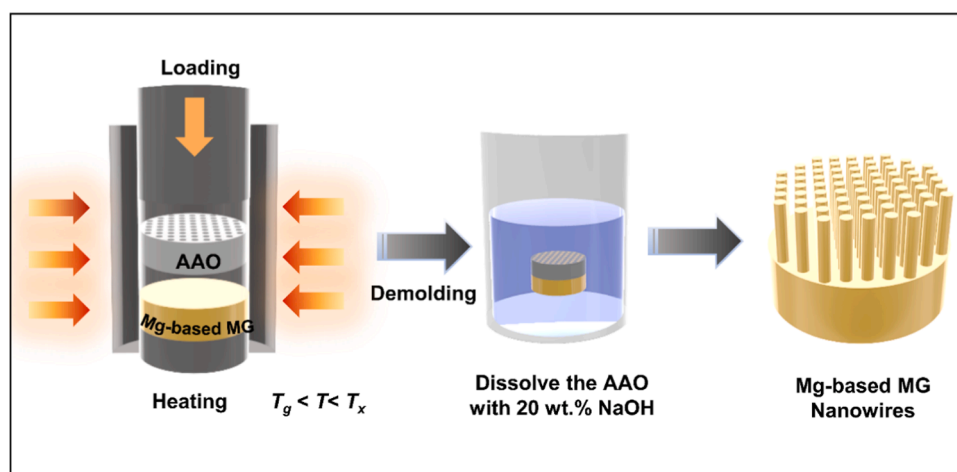


Fig. 1. Preparation route of Mg-based MG with NWs.

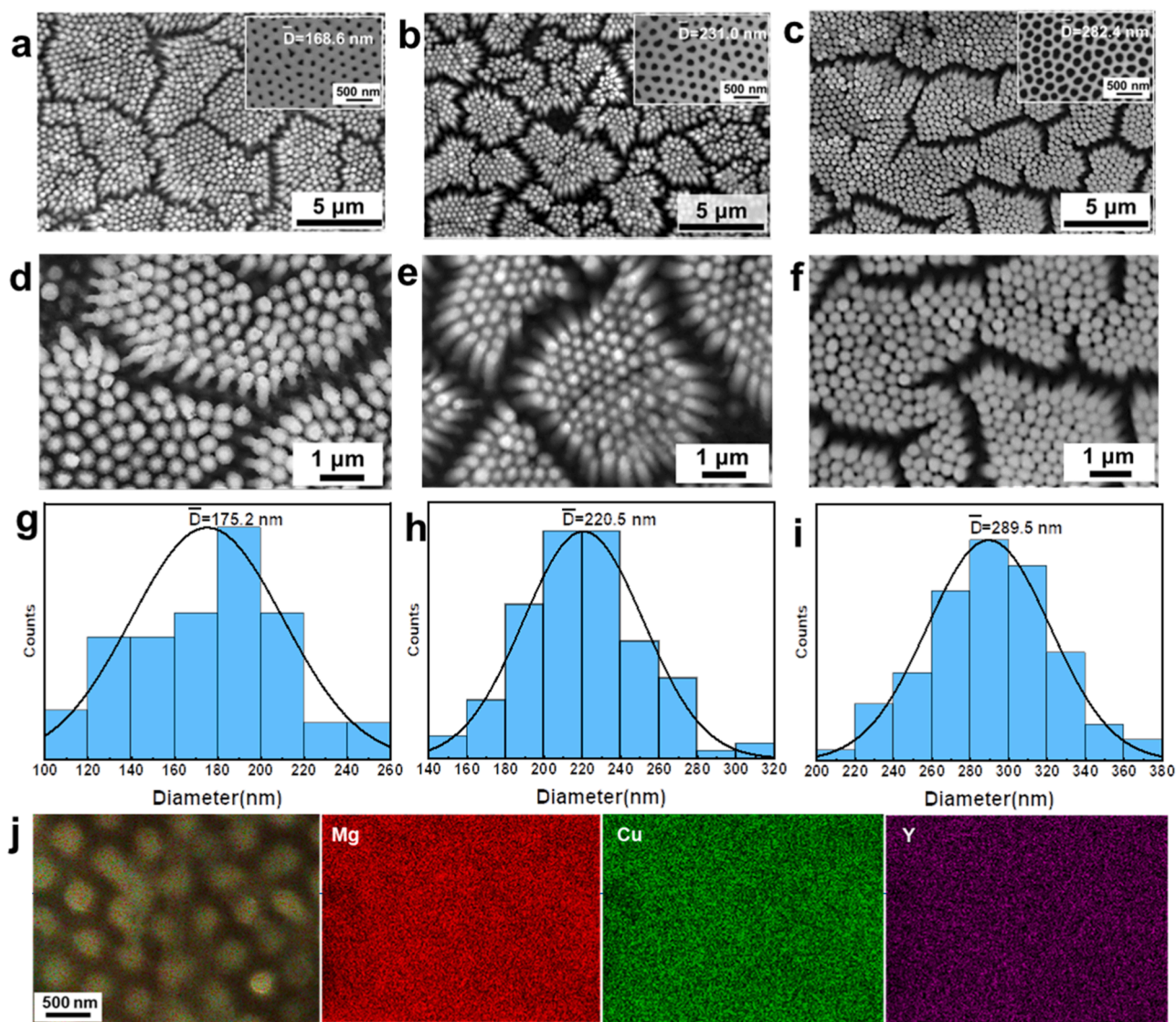


Fig. 2. (a)-(c) SEM morphology of NWs with diameters of 175 nm, 221 nm and 290 nm; (d)-(f) High magnification SEM images of NWs with diameters of about 175 nm, 221 nm and 290 nm; (g)-(i) Statistical distribution of diameter of three different NWs; (j) energy spectrum analysis of the Mg-based MG with NWs.

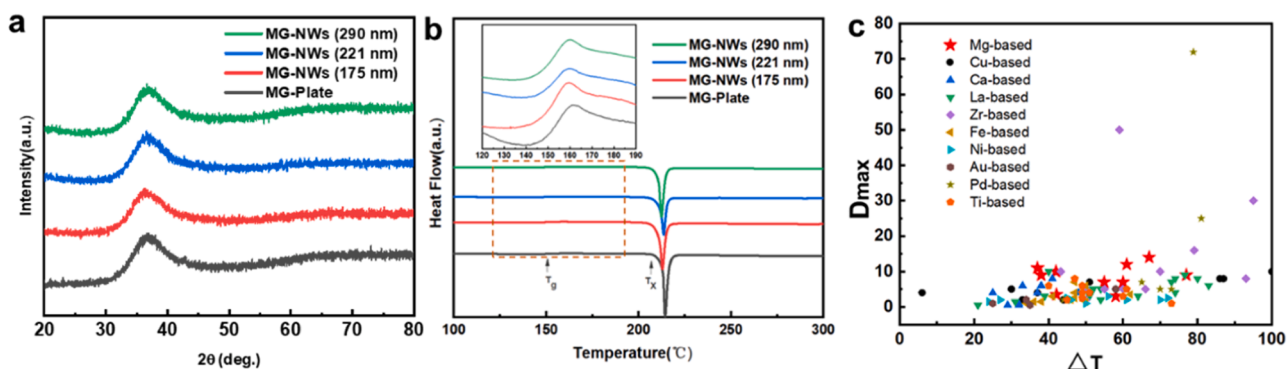


Fig. 3. (a) The XRD patterns of Mg-based MG after TPF; (b) The DSC curves of Mg-based MG after TPF; (c) Comparison of the SCLR and critical size of Mg-based MG with other MG systems [38,39].

$$h_j = \zeta \frac{v^2}{22g} \quad (1)$$

where ζ is the local head loss coefficient, determined by experiments,

and v is the average flow velocity of the section corresponding to ζ .

The Reynolds number Re is used in fluid mechanics to characterize the ratio of the inertial force and the viscous force to the moving fluid particles, and is used to measure the flow state of the fluid.

Table 1
DSC results comparison of different samples.

Samples	T_g (°C)	T_x (°C)	$\Delta T = T_x - T_g$ (°C)
MG-Plate	152	205	53
MG-NWs (175 nm)	149	204	55
MG-NWs (221 nm)	148	204	56
MG-NWs (290 nm)	149	203	54

$$Re = \frac{\rho u D}{4 \mu} \quad (2)$$

In the equation, ρ represents the fluid density, u is the fluid velocity, D is the diameter of NWs, μ is the viscosity of Mg-based MG.

For the Mg-based MG hot pressing process, take $\rho \approx 1.8 \times 10^3 \text{ kg m}^{-3}$, $u = 5 \text{ } \mu\text{m s}^{-1}$, $D \approx 300 \text{ nm}$, $\mu \approx 10^6 - 10^8 \text{ Pa s}$, $Re \approx 10^{-14} - 10^{-16} \ll 1$, The critical Reynolds number is based on the Schiller experimental value $Re_c = 2300$. When $Re < Re_c = 2300$, it is laminar flow, so Mg-based MG Newtonian fluid belongs to laminar flow state [42]. According to the Hagen-Poiseuille equation, the MG is an incompressible Newtonian fluid in a laminar state in the template. The supercooled liquid satisfies the following equation:

$$\Delta p = p - p_2 = \frac{32 \mu L^2}{t D^2} \quad (3)$$

The additional pressure P_2 [43] generated by the radial component of the capillary at the front end of the supercooled liquid is:

$$p_2 = - \frac{4 \gamma \cos \theta}{D} \quad (4)$$

Therefore, the viscous force caused by the viscosity of the supercooled liquid and the capillary resistance caused by the surface tension work together along the pore axis during the TPF process:

$$P = \frac{32 \mu L^2}{t D^2} - \frac{4 \gamma \cos \theta}{D} \quad (5)$$

where L is the length of the liquid, t is the time required for the liquid to flow through the length L , γ is the interface energy, and θ is the wetting angle between the MG supercooled liquid and the template cavity. Using the parameters in Eq. (3) ($L/D \approx 3$, $\gamma \approx 1 \text{ N m}^{-1}$, $t \approx 60 \text{ s}$, $\theta = 140^\circ$) [44]. The capillary resistance to be overcome by the calculation of nanowire forming is 490 MPa, which is basically consistent with the pressure

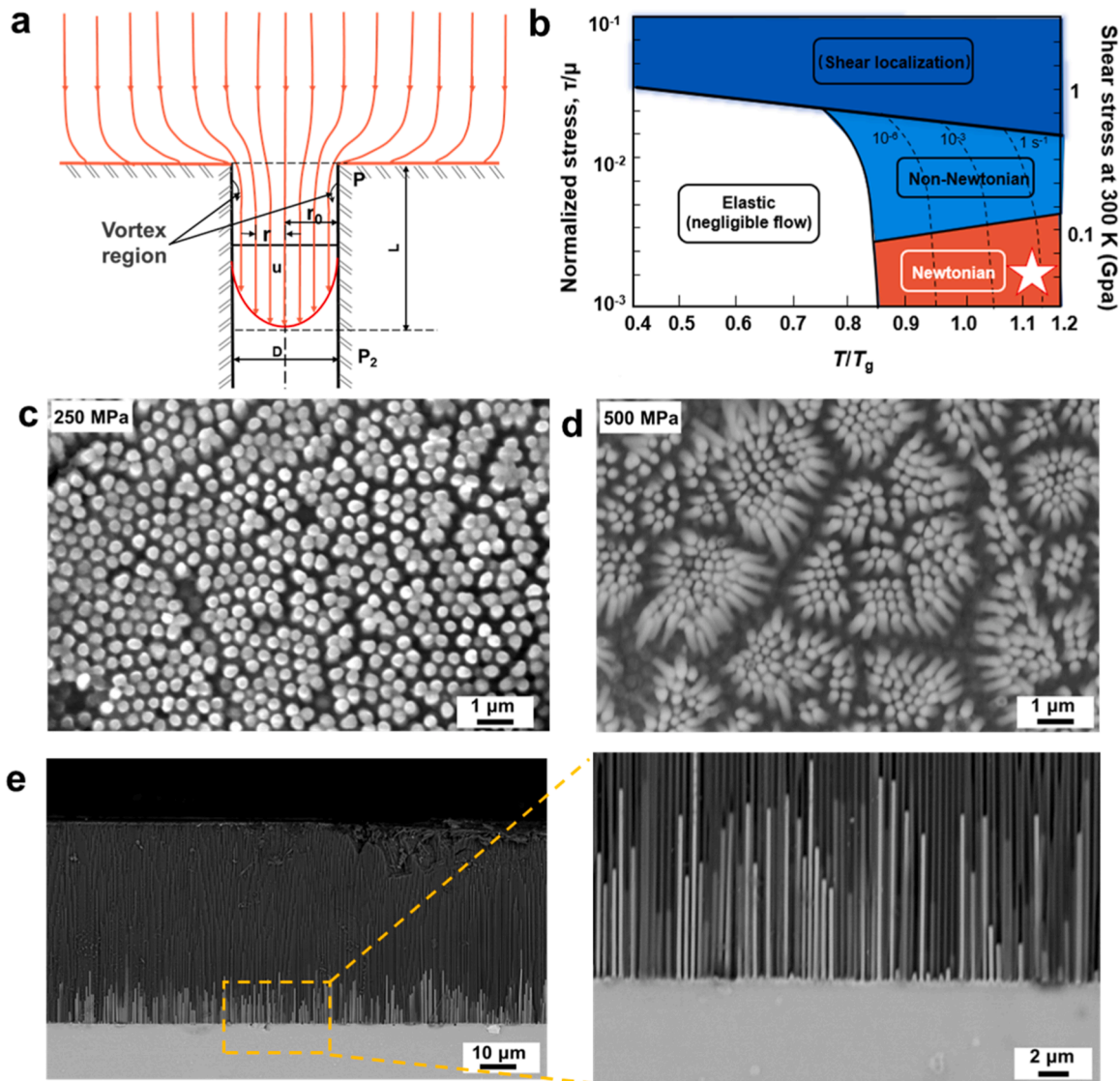


Fig. 4. (a) Schematic diagram of the filling process of Mg-based MG in AAO; (b) deformation diagram of MG under stress-temperature; (Data in Fig. 4b are taken from ref [45]. The hallow five-pointed star represents the parameters used in present research); (c) SEM morphology of NWs in 250 MPa pressure forming; (d) SEM morphology of NWs in 500 MPa pressure forming; (e) SEM morphological side view of NWs with a diameter of 221 nm in 1000 MPa pressure forming.

applied during the TPF process.

As shown in Fig. 4(b), the filling behavior of Mg-based MG in the template cavity is a fluid flow behavior. Referring to the MG stress-temperature deformation diagram of Schuh, C. [45], Fig. 4(b) is divided into four regions, shear region, elastic deformation region, non-Newtonian fluid region and Newtonian fluid region. In the figure, the orange area is the temperature-stress relationship of Newtonian fluid, and the pentagram is the corresponding temperature and stress in the preparation of NWs in the Mg-based MG SCLR. Fig. 4(c) shows the SEM morphology of NWs after TPF with AAO with a diameter of 221 nm at 250 MPa pressure. Fig. 4(d) shows the SEM morphology of NWs after TPF at 500 MPa pressure. As can be seen from the figure, the length of NWs increases with the increase of pressure, and the aspect ratio of NWs can reach 7 under the pressure of 500 MPa. Fig. 4(e) shows the filling of NWs into the AAO template at 1000 MPa pressure, from which it can be

seen that the NWs length-to-diameter ratio can reach more than 30.

Fig. 5(a) shows the schematic diagram of the MG with NWs heating up under laser irradiation at a wavelength of 808 nm. When the frequency of the incident light coincides with the resonance frequency of free electrons in the metal, the metal nanoparticles will have a strong extinction effect on this part of the light, resulting in the localized surface plasmon resonance effect [46]. The absorbed energy is mainly converted into heat and released and utilized, resulting in photothermal effect [47–49], which increases the surface temperature of the sample. Nanoparticles with photothermal effect can be applied to photothermal therapy of cancer. For the biocompatibility of one of the rare earth elements Y, H. Li and O. Baulin [40,50] studied the effect of adding Y to alloys on biocompatibility and found that it did not exhibit biotoxicity and was even beneficial for cell proliferation, so Y could be added as an alloying element to biodegradable metals. Due to the biocompatibility of

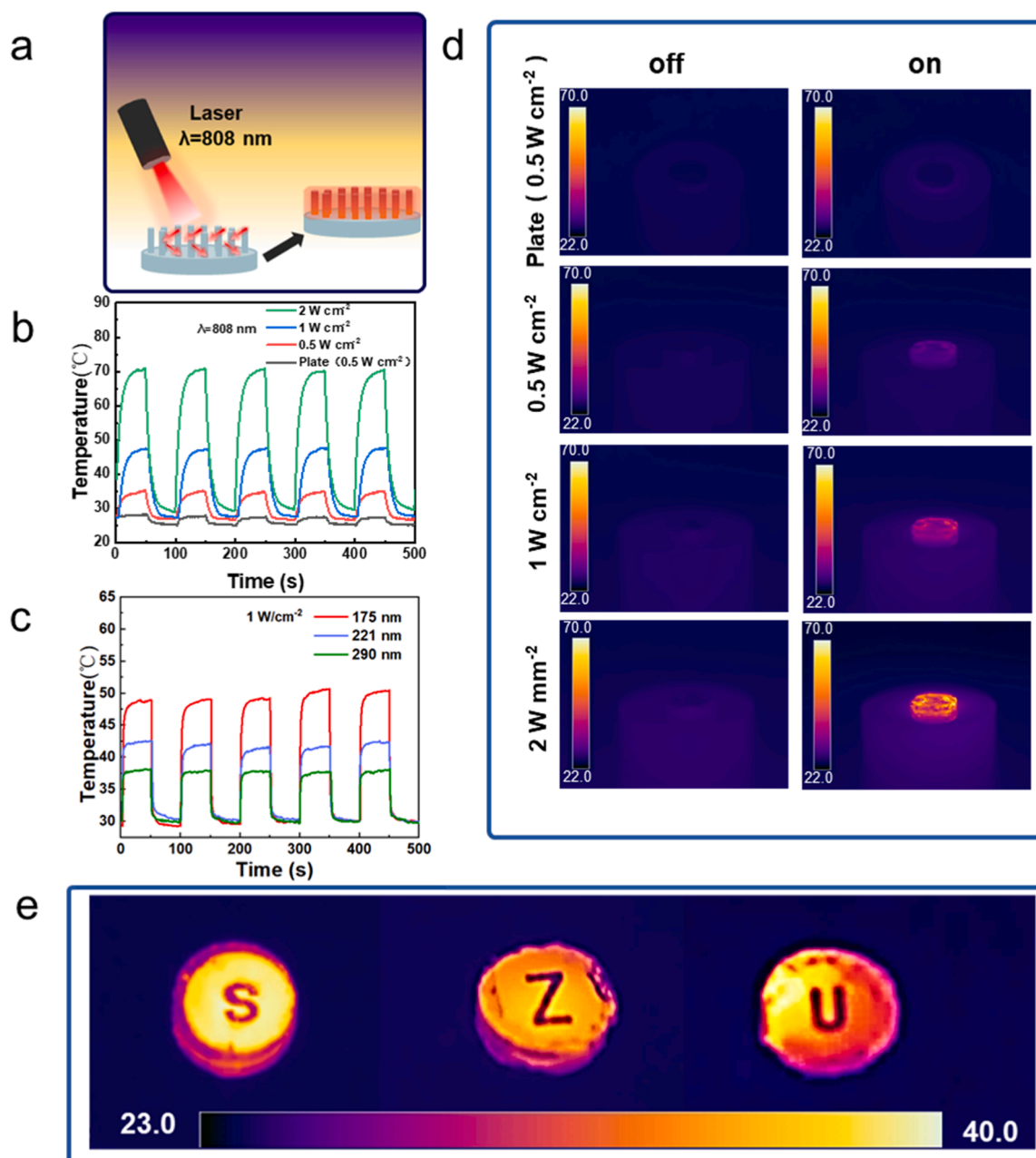


Fig. 5. (a) Illustration of photothermal effect of NWs; (b) Temperature rise rate curve under different laser powers; (c) Temperature rise rate curve for NWs of different diameters under 1 W cm⁻² laser irradiation; (d) Infrared thermal imaging of sample surface under different laser powers; (e) Infrared thermal image with SZU abbreviation.

Mg-based MG and the photothermal effect of NWs prepared by TPF, Mg-based MG NWs have great prospects in the field of photothermal therapy.

The NIR [51] region of the spectrum is known as the “therapeutic window” [52,53] due to the ability of NIR light to penetrate deep into human tissue. Fig. 5(b) shows the temperature change curves of MG with smooth surface and 290 nm diameter NWs samples under different power laser irradiation at 808 nm NIR wavelength. The surface temperature of the smooth sample remains essentially at an ambient temperature of 27 °C under 50-second intervals of laser irradiation. However, samples with NWs had different heating rates of 0.6 °C s⁻¹, 2.5 °C s⁻¹, 4.6 °C s⁻¹ and surface temperatures of ~35 °C, ~47 °C and ~71 °C under irradiation at 0.5 W cm⁻², 1 W cm⁻² and 2 W cm⁻², respectively. Fig. 5(c) shows the temperature variation curves of three different diameters of NWs samples under 1 W cm⁻² laser irradiation. The maximum temperatures of NWs with diameters of 175, 221 and 290 nm were ~50 °C, ~42 °C and ~38 °C. The reason for this is that as the diameter becomes smaller, the local surface plasmon resonance effect is stronger, resulting in a more superior photothermal effect.

Fig. 5(d) shows the infrared thermal imaging of the sample under different NIR laser power irradiation [52]. When the sample is not irradiated by laser, the sample temperature is essentially the same as the ambient temperature. When the sample is irradiated by laser, the surface temperature of the sample without NWs structure remained essentially unchanged, while the surface temperature of the sample with NWs increases with increase power. Fig. 5(e) shows the infrared thermal imaging of SZU, the representative letter of ShenZhen University. The temperature of the part around the letter is higher because of the NWs, while the temperature of the letter part is lower because of the absence of NWs.

In summary, we successfully fabricated Mg-based MG NWs with different diameters by TPF. In addition, the Newtonian fluid behavior of the NWs in the TPF process is also investigated. Due to the unique nanostructure of the surface, Mg-based NWs have excellent photothermal effect, and the surface temperature of the sample can reach 71 °C under the irradiation of NIR laser with a power of 2 W cm⁻² in a short time of about 20 s. As the diameter of the NWs decreases, the maximum temperature is higher and the photothermal effect is more obvious. Our work provides a novel approach to fabricate low-cost and biocompatible nanowire structures, and the nanowire photothermal effect holds great prospect in cancer photothermal therapy.

Declaration of Competing Interest

The authors declare that they have no known competing financial interests or personal relationships that could have appeared to influence the work reported in this paper.

Acknowledgments

The work was supported by the Key Basic and Applied Research Program of Guangdong Province, China (Grant nr. 2019B030302010), the NSF of China (Grant nr. 52122105, 51871157, 51971150), the National Key Research and Development Program of China (Grant no. 2018YFA0703604). The authors also thank the assistance on microscope observation received from the Electron Microscope Center of Shenzhen University.

References

- [1] S.P. Sharma, P. Goyal, *Mater. Today: Proc.* 28 (2020) 1593–1597.
- [2] C. Li, J. Qiu, J.-Y. Ou, Q.H. Liu, J. Zhu, A.C.S. *Appl. Nano Mater.* 2 (5) (2019) 3231–3237.
- [3] S.A. Theofanidis, V.V. Galvita, C. Konstantopoulos, H. Poelman, G.B. Marin, *Mater. (Basel)* 11 (5) (2018).
- [4] J.X. Qian, T.W. Chen, L.R. Enakonda, D.B. Liu, J.-M. Basset, L. Zhou, *Int. J. Hydrogen Energy.* 45 (32) (2020) 15721–15743.
- [5] J. Ju, J. Ma, Y. Wang, Y. Cui, P. Han, G. Cui, *Energy Storage Mater* 20 (2019) 269–290.
- [6] M. Zhou, X. Xiong, B. Jiang, C. Weng, *Appl. Surf. Sci.* 427 (2018) 854–860.
- [7] S. Quiles-Díaz, Y. Martínez-Rubí, J. Guan, K.S. Kim, M. Couillard, H.J. Salavagione, M.A. Gómez-Fatou, B. Simard, *Appl. Surf. Sci.* 2 (1) (2018) 440–451.
- [8] G. Williams, M. Hunt, B. Boehm, A. May, M. Taverne, D. Ho, S. Giblin, D. Read, J. Rarity, R. Allenspach, S. Ladak, *Nano Res* 11 (2) (2017) 845–854.
- [9] R.F. Pease, S.Y. Chou, *Proc. IEEE* 96 (2) (2008) 248–270.
- [10] R. Winkler, J.D. Fowlkes, P.D. Rack, H. Plank, *J. Appl. Phys.* 125 (21) (2019).
- [11] I. Utke, A. Luisier, P. Hoffmann, D. Laub, P.A. Buffat, *Appl. Phys. Lett.* 81 (17) (2002) 3245–3247.
- [12] H. Palneedi, J.H. Park, D. Maurya, M. Peddigari, G.T. Hwang, V. Annapureddy, J. W. Kim, J.J. Choi, B.D. Hahn, S. Priya, K.J. Lee, J. Ryu, *Adv Mater* 30 (14) (2018), e1705148.
- [13] H. Le, P. Penchev, A. Henrottin, D. Bruneel, V. Nasrollahi, J.A. Ramos-de-Campos, S. Dimov, *Micromachines (Basel)* 11 (2) (2020).
- [14] J. Schroers, T.M. Hodges, G. Kumar, H. Raman, A.J. Barnes, Q. Pham, T.A. Waniuk, *Mater. Today.* 14 (1–2) (2011) 14–19.
- [15] J. Ma, X.Y. Zhang, D.P. Wang, D.Q. Zhao, D.W. Ding, K. Liu, W.H. Wang, *Appl. Phys. Lett.* 104 (17) (2014).
- [16] Z. Li, J. Ma, *Mater. Today Adv.* 12 (2021).
- [17] M.N. Avettand-Fénoël, N. Netto, A. Simar, M. Marinova, R. Taillard, *J. Alloys Compd.* 907 (2022).
- [18] H. Lin, J. Yang, H. Zhao, J. Gou, Y. Zhang, J. Fu, F. Sun, W. Ruan, Z. Zhang, X. Liang, S. Ren, T. Ma, J. Ma, J. Ma, J. Shen, *Intermetallics* 145 (2022).
- [19] J. Li, G. Doubek, L. McMillon-Brown, A.D. Taylor, *Adv Mater* 31 (7) (2019), e1802120.
- [20] F.-Y. Chang, C.-Y. Cheng, S.-W. Chau, J.P. Chu, Y.-C. Chen, *Intermetallics* 30 (2012) 35–39.
- [21] A. Inoue, A. Takeuchi, *Acta Mater.* 59 (6) (2011) 2243–2267.
- [22] A. Ks, J. Tian, J. Shen, *Chin. Chem. Lett.* (2021).
- [23] S. Zhang, C. Wei, L. Yang, J. Lv, Z. Shi, H. Zhang, X. Zhang, M. Ma, *J. Non-Cryst. Solid.* 587 (2022).
- [24] X. Mu, M.R. Chellali, E. Boltynjuk, D. Gunderov, R.Z. Valiev, H. Hahn, C. Kubel, Y. Ivanisenko, L. Velasco, *Adv Mater.* 33 (12) (2021), e2007267.
- [25] P. Zhang, J.J. Maldonis, Z. Liu, J. Schroers, P.M. Voyles, *Nat Commun* 9 (1) (2018) 1129.
- [26] G. Doubek, R.C. Sekol, J. Li, W.-H. Ryu, F.S. Gittleston, S. Nejadi, E. Moy, C. Reid, M. Carmo, M. Linardi, P. Bordeenithikasem, E. Kinser, Y. Liu, X. Tong, C.O. Osuji, J. Schroers, S. Mukherjee, A.D. Taylor, *Adv. Mater.* 28 (10) (2016) 1940–1949.
- [27] T. Ichitsubo, E. Matsubara, T. Yamamoto, H.S. Chen, N. Nishiyama, J. Saida, K. Anazawa, *Phys. Rev. Lett.* 95 (24) (2005), 245501.
- [28] X. Liu, Y. Shao, Z. Han, K. Yao, *Sci. Bull.* 60 (6) (2015) 629–633.
- [29] R.C. Sekol, M. Carmo, G. Kumar, F. Gittleston, G. Doubek, K. Sun, J. Schroers, A. D. Taylor, *Int. J. Hydrogen Energy.* 38 (26) (2013) 11248–11255.
- [30] G. Kumar, A. Desai, J.J.A.M. Schroers, *Adv. Mater.* 23 (4) (2011) 461–476.
- [31] G. Qu, T. Xia, W. Zhou, X. Zhang, H. Zhang, L. Hu, J. Shi, X.F. Yu, G. Jiang, *Chem Rev* 120 (4) (2020) 2288–2346.
- [32] S. Ren, H.X. Zong, X.F. Tao, Y.H. Sun, B.A. Sun, D.Z. Xue, X.D. Ding, W.H. Wang, *Nat. Commun.* 12 (1) (2021) 5755.
- [33] C. Wang, S.S. Rubakhin, M.J. Enright, J.V. Sweedler, R.G. Nuzzo, *Adv. Funct. Mater.* 31 (14) (2021), e2000619.
- [34] D. Zhao, Y. Zhu, W. Cheng, W. Chen, Y. Wu, H. Yu, *Adv. Mater.* 33 (28) (2021), e2000619.
- [35] M. Dambatta, S. Izman, B. Yahaya, J. Lim, D. Kurniawan, *J. Non-Cryst. Solid.* 426 (2015) 110–115.
- [36] S.J.B. Bin, K.S. Fong, B.W. Chua, M.J.J.o.M. Gupta, *Alloys, J. Magnesium Alloys.* (2021).
- [37] A. Sharma, A. Kopylov, M. Zadorozhnyy, A. Stepashkin, V. Kudelkina, J.-Q. Wang, S. Ketov, M. Churyukanova, D. Louzguine-Luzgin, B. Sarac, J. Eckert, S. Kaloshkin, V. Zadorozhnyy, H. Kato, *Metals (Basel)* 10 (7) (2020).
- [38] J. Schroers, W.L. Johnson, *Appl. Phys. Lett.* 84 (18) (2004) 3666–3668.
- [39] Z. Long, H. Wei, Y. Ding, P. Zhang, G. Xie, A. Inoue, *J. Alloy. Compd.* 475 (1–2) (2009) 207–219.
- [40] H. Li, P. Wang, G. Lin, J. Huang, *Acta Biomater* 129 (2021) 33–42.
- [41] C.A. Schuh, T.C. Hufnagel, U.J.A.M. Ramamurty, *Acta Mater.* 55 (12) (2007) 4067–4109.
- [42] A.S. Berman, *J. Appl. Phys.* 24 (9) (1953) 1232–1235.
- [43] G. Kumar, H.X. Tang, J.J.N. Schroers, *Nat* 457 (7231) (2009) 868–872.
- [44] Q. Liao, C. Mu, D.-S. Xu, X.-C. Ai, J.-N. Yao, J.-P.J.L. Zhang, 25(8) (2009) 4708–4714.
- [45] C. Schuh, T. Hufnagel, U. Ramamurty, *Acta Mater.* 55 (12) (2007) 4067–4109.
- [46] X. Fan, L. Liu, X. Jin, W. Wang, S. Zhang, B. Tang, *J. Mater. Chem. A.* 7 (23) (2019) 14319–14327.
- [47] D. Xu, Z. Li, L. Li, J. Wang, *Adv. Funct. Mater.* 30 (47) (2020).
- [48] L. Zhao, Y. Liu, R. Xing, X. Yan, *Angew. Chem. Int. Ed. Engl.* 59 (10) (2020) 3793–3801.
- [49] J. Chen, C. Ning, Z. Zhou, P. Yu, Y. Zhu, G. Tan, C. Mao, *Prog. Mater. Sci.* 99 (2019) 1–26.
- [50] O. Baulin, M. Bugnet, D. Fabrègue, A. Lenain, S. Gravier, S. Cazottes, G. Kapelski, B. Ter-Ovanesian, S. Balvay, D.J. Hartmann, J.-M. Pelletier, *Mater.* 1 (2018) 249–257.
- [51] M. Kim, J.H. Lee, J.M. Nam, *Adv. Sci. (Weinh)* 6 (17) (2019), 1900471.
- [52] S. Wu, H.J. Butt, *Adv. Mater.* 28 (6) (2016) 1208–1226.
- [53] P.C.A. Swamy, G. Sivaraman, R.N. Priyanka, S.O. Raja, K. Ponnuel, J. Shanmugpriya, A.J.C.C.R. Gulyani, *Coord. Chem. Rev.* 411 (2020), 213233.